

## Effects of confinement on absolute and convective instabilities for momentum-driven countercurrent shear layers

Jinwei Yang, Matt J. Anderson, Paul J. Strykowski, and Vinod Srinivasan \*

Department of Mechanical Engineering, University of Minnesota, Minneapolis, Minnesota 55455, USA



(Received 22 October 2020; accepted 7 May 2021; published 6 July 2021)

Using spatiotemporal linear stability theory, we conduct a systematic study of confined countercurrent shear layer velocity profiles, using realistic velocity profiles that capture the effects of wall boundary layers on canonical profile shapes. It is shown, in line with previous studies, that additional unstable modes are generated when confining walls are present. This leads to shifts in the absolute-convective transition boundary, with the effects being dramatic when confinement is on the high-speed side. However, over large parts of the parameter space, as specified by the counterflow parameter  $R$  and the degree of confinement ( $H$ , measured in terms of shear layer momentum thickness), these correspond to long wave modes. It is shown that as counterflow parameter  $R$  ( $= \frac{U_1 - U_2}{U_1 + U_2}$ ,  $U_1$  and  $U_2$  being primary and secondary velocity streams) is increased to large values, the confined mode gradually decreases in wavelength. Comparisons of the behavior of the frequency of this confined mode are made with observed peak frequencies from the first experimental realization of momentum-driven confined countercurrent shear layers, and the results are shown to be in reasonable agreement.

DOI: [10.1103/PhysRevFluids.6.073901](https://doi.org/10.1103/PhysRevFluids.6.073901)

### I. INTRODUCTION

Flame anchoring in combustors is often accomplished by the use of sudden expansions or bluff-body wakes, producing a region of recirculation with energetic turbulence. This region exhibits a large reverse velocity, up to 20% of the forward velocity, and produces vortical structures that promote flame wrinkling [1,2]. Investigators have exploited this effect by applying suction in the recirculation region, further enhancing the reverse flow, with dramatic enhancements in heat release rate and reductions in flame length [3]. The onset of this enhanced mixing regime is accompanied by self-sustained oscillations with frequencies that depend in a complex manner on the geometry and operating conditions: the density and velocity fields, which in turn are closely linked to the local distribution of heat release [4]. If this hydrodynamically driven frequency is too close to the acoustic frequency of the confining duct, and if heat release rate oscillations occur sufficiently in phase with pressure oscillations, then thermoacoustic instabilities may result, causing large, undesirable pressure fluctuations and eventual flame blow-off. Therefore, *a priori* knowledge of these hydrodynamic frequencies is valuable to the designer.

More generally, mixing layers occur in a large variety of natural and engineering situations and are of interest as they also serve as a basic building block appearing in other flows such as wakes, jets, and recirculating flows. It is now well recognized that free shear layers with significant reverse velocities exhibit a regime with global modes characterized by high rates of mixing, self-sustained oscillations at a frequency that is observed everywhere in the domain, an absence of receptivity to external forcing, and a sharp onset from a previous laminar or low-turbulence

---

\*vinods@umn.edu

state. Such countercurrent mixing layers are known to be members of a class of globally unstable flows, which include bluff-body wakes [5], low-density jets [6], core-annular flows [7], and swirling flows [8]. In each case, the steep transition to the unstable regime is controlled by a relevant flow parameter, such as the jet-ambient density ratio [9], countercurrent velocity ratio [10], or velocity defect [11]. The experimental observations of the onset of these global modes have been explained by theoretical studies that examine the spatiotemporal linear stability of local velocity and/or density profiles in an appropriate upstream region of the flow where the flow is weakly nonparallel. The predictions of linear theory for the frequencies of the most unstable modes in countercurrent shear layers, low-density jets and bluff-body wakes, have been shown to closely track the discrete frequencies of observed self-sustained oscillations in these flows [12–14]. For the specific case of a countercurrent mixing layer with a primary flow stream of velocity  $U_1$ , Strykowski and Niccum [10] demonstrated that the onset of the global mode occurred as the secondary (reverse) velocity  $U_2$  was increased beyond a critical velocity ratio of  $\frac{U_2}{U_1} = -13.6\%$ , or equivalently for  $R = (U_1 - U_2)/(U_2 + U_1) > 1.315$ , closely matching the predictions of Huerre and Monkewitz [12]. It is conjectured that locally absolute unstable profiles established over a small but finite region can act as a wavemaker, generating instabilities which grow in time and space, eventually permeating the entire domain and leading to a strongly nonlinear breakdown [15,16]. Here, absolute instability refers to the presence of unstable modes of zero group velocity but with positive amplification rate, as calculated from local profiles using spatiotemporal linear theory. Numerically, a set of velocity, density, and viscosity profiles is said to be absolutely unstable if the dispersion relation for a wave packet displays a saddle point in the complex wave-number plane with a positive growth rate that also corresponds to the amplification of upstream- and downstream-traveling waves [17,18]. The surprisingly good match between spatiotemporal linear theory and measurements for flows which undergo strongly nonlinear breakdown and saturate in an enhanced turbulent mixing regime has been explained to be the result of the breakdown process being driven by a mode which originates in a linear mechanism.

Examining the mixing characteristics of global modes in pressure-driven countercurrent shear layers has proven difficult in the laboratory. The experiments of Humphrey and Li [19] were the first attempt to create a pressure-driven countercurrent shear layer in a confined environment. Splitter plates were used in a modified wind tunnel to separate opposing streams on opposing transverse sides of the plates. The expectation that a countercurrent shear layer would be established in the streamwise space between the plates was belied; strong transverse pressure gradients were established, and a stagnation point was observed between the splitter plates, with no streamwise extensive counterflow. The inability to establish opposing velocity streams over a sufficiently extended domain was attributed to the strong confinement of the bounding walls used to contain and direct the flow. Strykowski and Niccum [10] were the first to experimentally establish a spatially evolving countercurrent mixing layer with significant streamwise extent, which they achieved by eschewing momentum-driven counterflow and instead applying suction around the periphery of a circular jet. Subsequently, Forliti and co-workers [20,21] extended the idea of creating suction-driven counterflowing velocity profiles to a confined planar geometry, demonstrating the loss of similarity in transverse profiles of turbulent shear stresses at large downstream distances, as counterflow was increased. The enhanced mixing rates afforded by such a flow configuration [20] were used by Behrens and Strykowski [3] to enhance heat release rates in a dump combustor. While such studies demonstrated that counterflowing velocity profiles indeed enhanced mixing, they are not attractive from an engineering perspective, and momentum-driven counterflow remains a goal.

Recently, Anderson [22] described measurements in a facility for establishing partially confined momentum-driven countercurrent shear flows, based on use of the Coanda effect to promote attachment of one of the counterflowing streams to the wall, preventing a stagnation point flow. He showed that by moving the secondary air jet closer or farther away from the splitter plate defining the primary stream, a nearly uniform countercurrent shear layer could be created, which exhibited the hallmarks of global modes, such as high turbulence levels, discrete peaks in the frequency spectrum, and insensitivity to acoustic forcing. However, the experiment does deviate from the canonical

situation studied by Huerre and Monkewitz [12] of a free shear layer, instead featuring bounding walls, boundary layers, and streamline curvature. The dependence of the observed frequencies and wavelengths selected by the flow in such a situation is not clear, and is the focus of this study. The paper is structured as follows: Section II discusses the deviations of measured profiles from the canonical shear layer, Sec. III presents the problem formulation and numerical solution, Secs. IV and V examine the effects of wall confinement and boundary layer development on the unstable frequencies, and Sec. VI compares the predictions of theory with experimental observations of Anderson [22]. Some conclusions are discussed in Sec. VII.

## II. CONFINED SHEAR FLOWS

We recall that the canonical unconfined shear layer velocity profile studied by Huerre and Monkewitz [12] is defined as

$$U(y) = 1 + R \tanh\left(\frac{y}{2}\right), \quad (1)$$

which leads to forward and reverse velocities of  $1 + R$  and  $1 - R$ , respectively. A value of  $R = 1$  corresponds to a single stream mixing layer with quiescent fluid downstream of a splitter plate;  $0 < R < 1$  corresponds to two co-flowing streams. A value of  $1 < R < \infty$  implies counterflow, with the magnitude of the reverse (secondary) velocity approaching that of the primary stream for large  $R$ . The length scale used to scale distances in the transverse direction is the momentum thickness, obtained by integration of the above velocity profile, which yields the numeric value of unity. The velocity scale is the velocity at the center of the mixing layer ( $y = 0$ ), which is also the location of the inflection point in the profile, and hence the point with maximum velocity gradient. For a constant density, this canonical velocity profile exhibits absolute instability when the reverse velocity exceeds the fraction 0.136 of the forward velocity ( $R = 1.315$ ), reflected in the emergence of a saddle point in contours of the complex frequency  $\omega$  when plotted on the complex wave-number ( $k$ ) plane. While experimental observations of the onset of global modes [10] have validated theoretical predictions of the critical counterflow ratio  $R$  required for absolute instability [12], there are no experimental data available that document the effects of confinement, which is relevant to practical applications. For guidance on the anticipated behavior of a confined countercurrent mixing layer, one would anticipate that the predictions of linear theory will provide a reasonable initial approximation. Juniper [23] studied an idealized case of three inviscid streams with plug flow profiles and confined by walls on two sides. He noted the emergence of additional saddle points in the complex plane corresponding to confinement. For certain combinations of velocity and density profiles, the confined modes could become more unstable than the erstwhile dominant mode. The interaction between two unstable modes could also lead to shifts in the absolute-convective transition boundary in the relevant parameter space. This matches well with the observations of Bearman and Zdravkovich [24], who found that as a long cylinder was brought closer to the wall, the frequency of Bénard–von Kármán vortex shedding became irregular, before becoming well defined again as the wall separation was further reduced.

Healey [25] pointed out that far from the shear layer, where  $U'' = 0$ , the inviscid Rayleigh equation reduces to  $v'' - k^2v = 0$ , which ordinarily would imply negative values of  $k$  (exponential decay away from the shear layer) to satisfy far-field conditions, but admits positive values in the presence of a confining wall. As a result, the presence of a wall on the high-speed or low-speed side causes the emergence of multiple saddle points in the complex wave-number plane, which are an integer multiple of the largest possible wave number in the transverse direction between the shear layer and the confining wall. In the compressible situation, this would correspond to the formation of acoustic standing waves of multiple wavelengths between the wall and the shear layer inflection point location. A long-wave approach suggested that despite the stabilizing effects of confinement on temporal stability, the effects on absolute stability can be quite dramatic. The long-wave modes have significant positive growth rates in the presence of confinement, leading to

absolute instability for very low levels of counterflow,  $R < 1.32$ . In fact, for the case of confinement of the high-speed stream, absolute instability is predicted to be triggered for  $R = 0.998$ , i.e., when there is no counterflow. No change in the  $A$ - $C$  boundary was predicted for confinement on the low-speed side.

Long-wave modes had been previously found [23,26], but were dismissed as nonphysical. Koch [27] and Huerre and Monkewitz [12] had calculated unstable modes with negative  $k_r$  for  $R < 0.84$ , and also argued for disregarding them on physical grounds. Healey points out that such modes are physically admissible due to the relaxation of exponential decay in the presence of confining walls. However, Healey does not explicitly provide details on the wavelength of the modes as confinement is varied. Juniper [28] had also recognized the admissibility of additional varicose modes arising in a three-layer shear flow configuration that captures the essential features of planar inviscid jets and wakes. Juniper [28] pointed out that the response of the outer fluid layer may be different from that in the inner layer, if the flow develops quickly in the streamwise direction, which is likely in any experimental configuration featuring confinement. Questions remain over whether such unstable modes can be experimentally detected; wavelengths that are large relative to the shear layer thickness may not establish themselves over a sufficiently finite extent of the domain due to the weakly nonparallel nature of any experimentally realized flow. Thus, even if a long-wavelength mode is predicted to be absolutely unstable as a result of confinement, the experimentally observed instability may very well correspond to the less unstable, hitherto unconfined mode.

The question of wavelength selection in a real laboratory flow has been recently addressed by Arratia *et al.* [29]. Using a Legendre-type transform, they study the primary and secondary instabilities of a row of equally spaced point vortices symmetrically confined between two walls. These vortices represent the vortices issuing from the primary instability of the countercurrent shear layer, and are known to merge downstream in a pairwise manner, as documented by Winant and Browand [30]. This in turn leads to a secondary instability that is also absolute in nature [31]. Without confinement, this sequential merging can perpetuate itself, leading to larger and larger vortices with increasing separation while remaining absolutely unstable; however, the presence of confining walls implies that at some level of merging, the secondary instability due to these vortices will be strongly confined, causing a transition to convective instability. Arratia *et al.* conjecture that the primary instability may then lock onto this convectively unstable frequency, thereby constituting a frequency selection mechanism for confined shear layers. This leads to the conclusion that a confined counterflowing mixing layer can be achieved only with a long narrow test section, in which the distance of the wall from the shear layer is sufficiently large that the primary instability is not suppressed, while also being small enough relative to the downstream distance that the secondary instability has the space to establish itself. The lack of the long downstream distance may very well be the reason for the establishment of a stagnation point flow in the experiments of Humphrey and Li [19].

The above studies provide a qualitative description of expected behavior for a potential experimental realization of a planar counterflowing mixing layer. However, none of these studies captures real effects such as the role of viscosity, disturbed wall boundary layers, and any transverse pressure gradients that may be set up due to injection. As a result, the expected globally unstable frequency, which is of practical relevance in combustors, requires a full spatiotemporal analysis of measured profiles. Manoharan and Hemchandra [32] do carry out a study of shifts in the absolute-convective transition boundary for wall-bounded profiles downstream of a backward-facing step, including the effects of the density field. However, their velocity profiles were somewhat idealized, and the range of confinement was not large, with the emphasis being on the role of baroclinic effects. Therefore, we turn to the momentum-driven countercurrent shear layer experiments of Anderson [22] shown in Fig. 1, in which the secondary reverse flow was injected along a curved surface, with a radius of curvature two orders of magnitude larger than the shear layer thickness. Flow separation and stagnation point flow were not observed due to the stabilizing influence of the Coanda effect on the lower curved surface. Acoustic forcing was performed by connecting speakers through a duct to a cross section directly upstream of the splitter plate, where the shear layer starts to develop.

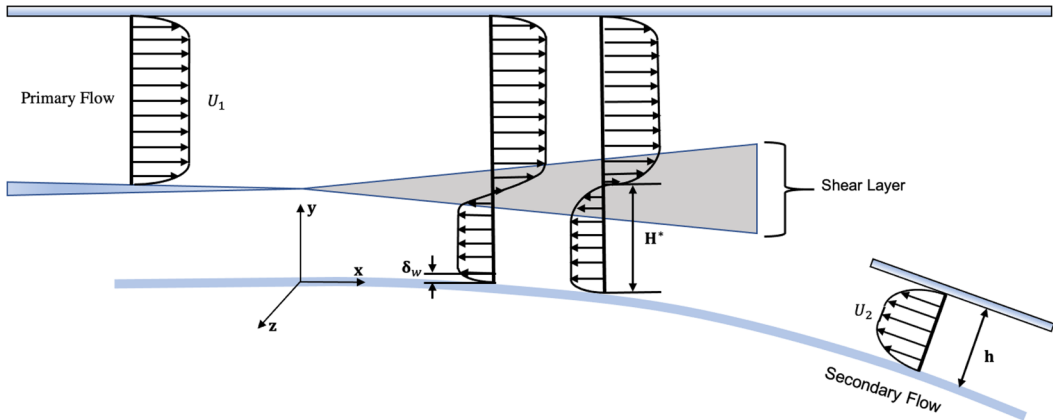


FIG. 1. Momentum-driven countercurrent shear layer facility used by Anderson [22].

Regimes of enhanced mixing were observed as the injection mass flow was increased, characterized by high turbulence levels and a peak in the frequency spectrum. The velocity spectra were sensitive to acoustic forcing at low injection flow rates, and fairly insensitive at higher flow rates, strongly suggesting the presence of global modes as shown in Fig. 84 of Ref. [22]. Consider the family of velocity profiles shown in Fig. 2, which were measured at the downstream location nearest to the splitter plate, for various values of the injected secondary mass flow. These profiles differ from the canonical case of a  $\tanh(y)$  profile in the following ways:

- (i) For large secondary mass flow rates, the maximum velocity magnitude occurs in the reverse direction.
- (ii) The secondary stream injection is accompanied by the development of a wall boundary layer, which progressively becomes thinner as the mass flow rate is increased.

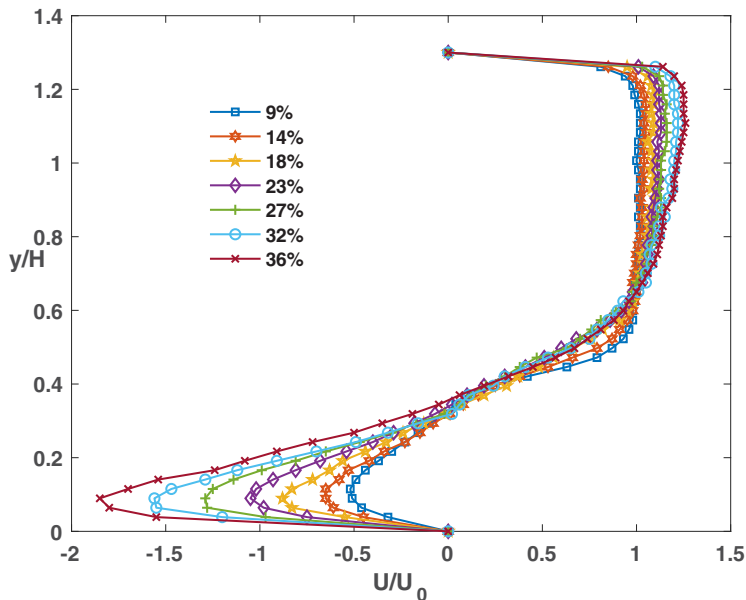


FIG. 2. Velocity profiles measured downstream of a splitter plate by Anderson [22].

TABLE I. Shear layer and boundary layer parameters evaluated from measured velocity profiles from the experiments by Anderson [22].

Mass flow rate (%)	$ \frac{U_2}{U_1} $	$\theta$ (mm)	$\delta^*$ (mm)	$\delta_w$ (mm)	$H^*$ (mm)	$R$	$f$ (Hz)
0.09	0.51	1.34	3.94	2.30	7.90	3.08	34.1
0.14	0.62	1.70	6.08	2.30	7.60	4.25	39.6
0.18	0.80	1.90	8.38	1.79	7.05	9.00	47.8
0.23	0.93	2.01	7.92	1.79	6.97	27.25	47.8
0.27	1.11	2.01	7.13	1.79	6.20	-18.85	28.3
0.32	1.18	2.14	6.7	1.79	5.80	-8.18	34.7
0.36	1.47	2.16	6.56	1.79	6.00	-5.27	41.5

(iii) The location of the inflection point of the velocity profiles moves progressively close to the wall with increased injection rates, accompanied by changes in the extent (and slope) of the countercurrent shear layer.

Table I summarizes these results. Distances are measured from the bottom wall along which the injected flow develops. A momentum thickness  $\theta$  is extracted from the measured velocity profiles by integrating over the shear layer down to the point of maximum reverse velocity  $U_2$ , but not into the wall boundary layer. Also calculated is a broader measure of the shear layer thickness  $\delta^*$ , based on the velocity difference between the primary and secondary streams, and the maximum velocity gradient in the shear layer. The location of the peak reverse velocity from the wall is assigned to  $\delta_w$ , the wall boundary layer thickness. The table also lists the value of  $R$  calculated from  $U_1$  and  $U_2$ , the location  $H^*$  of the inflection point, and the observed peak  $f$  in frequency.

### III. PROBLEM FORMULATION AND NUMERICAL APPROACH

#### A. Velocity profiles

Consideration of the velocity profiles in Fig. 2 suggests that three new length scales are introduced as a result of confinement in one direction:  $H^*$ ,  $\theta$ , and  $\delta_w$ . Choosing  $\theta$  as the length scale, we are left with two nondimensional parameters,  $H = \frac{H^*}{\theta}$  and  $\delta = \frac{\delta_w}{\theta}$ , which express the distance of the shear layer from the wall, and the boundary layer thickness, respectively. We also note the large magnitudes of  $R$ , exceeding 10 in some cases. We may potentially explore the relative merits of using  $\theta$  vs  $\delta^*$  as the appropriate length scale, since the instability originates from the point of maximum shear, rather than the integral length scale that characterizes the shear layer. For a canonical tanh profile, the ratio of these two quantities is fixed,  $\frac{\delta^*}{\theta} = 4$ , but is seen to vary in the measured profiles. We initially work with the momentum thickness, and consider the effects of  $\delta^*$  in Sec. VI.

Since the analytical profile in Eq. (1) cannot capture the situation where the secondary velocity is greater than that of the primary stream, we split the experimental profiles into two classes, one with  $|\frac{U_2}{U_1}| < 1$  corresponding to  $R > 1$ , and another with  $|\frac{U_2}{U_1}| > 1$  corresponding to  $R < -1$ . The base velocity profiles, without the wall boundary layer, are

$$U(y) = 1 + R \tanh \frac{y - H}{2}, \quad R > 1, \quad (2)$$

and

$$U(y) = -1 - R \tanh \frac{y - H}{2}, \quad R < -1, \quad (3)$$

with the momentum thickness implicitly set to 1, and not the dimensional value in Table I. The definition in Eq. (3) ensures that the primary velocity remains in the positive  $x$  direction. For an unconfined shear layer, the profiles for  $R > 1$  and  $R < -1$  are identical with a reflection of

coordinates; however, the presence of a wall breaks the symmetry and the two situations need to be considered separately. We note that a typical experimental approach, in which the forward velocity is fixed and the secondary flow is increased, would correspond to an increase in  $R$  from 1 to  $\infty$ . When the reverse velocity becomes greater than the forward velocity and continues to increase in magnitude, the value of  $R$  jumps from  $+\infty$  to  $-\infty$  and then increases towards  $-1$ .

### B. Solution procedure

To obtain the dominant wave disturbances for given velocity profiles, the Navier-Stokes equations are perturbed with two-dimensional velocity disturbances and linearized to yield a system of differential equations that encode the dispersion relation for the flow parameters  $(R, H, \delta)$ . This results in a generalized eigenvalue problem that is solved using Chebyshev collocation. Details of the numerical procedure and nonlinear mapping method are provided in the Supplemental Material [33]. Briefly, we expand the pressure and velocity disturbances in terms of Chebyshev polynomials and use a collocation method with appropriate mapping functions to obtain the frequency as a function of an input wave number:

$$\omega = \omega(k, R, H, \delta, \text{Re}). \quad (4)$$

We first discuss the effect of confinement of an inviscid countercurrent shear layer, using the profiles in Eqs. (2) and (3). Subsequently we present modifications to the above profiles that handle the effects of viscosity and the viscous wall boundary layer.

## IV. RESULTS

### A. $R > 1$ : Confinement on the low-speed side

The effect of  $H$  for  $R > 1$  has been studied elsewhere [25], but we explore the situation in some detail, paying attention to the frequencies and wavelengths of the most unstable mode. We first consider the case of  $R > 1$ , in which the near-wall stream is the low-speed flow. Starting from an unconfined countercurrent velocity profile that is just slightly supercritical ( $R = 1.315$ ), we track the saddle point location in the complex plane, as  $H$  is reduced from large values. Figure 3(a) shows the complex plane for  $H = 35$ , for which the dominant saddle point (marked  $S_1$ ) sits at a location  $k_0 = 0.1291 - 0.2395i$ , very close to the value of  $k_0 = 0.1291 - 0.2399i$  for the unconfined planar shear layer studied by Huerre and Monkewitz [12] for  $R = 1.315$ . As  $H$  is reduced to 25, we see the emergence of a long-wave mode (marked  $S_2$ ) of low  $k_r$ , whose saddle point location moves rightward, toward shorter wavelengths. Values of  $\omega_i$  for this  $S_2$  mode are positive; meanwhile, the growth rate of the unconfined  $S_1$  mode is close to zero. As  $H$  is reduced to 15 as shown in Fig. 3(c), this hitherto long-wave mode  $S_2$  has a shortened wavelength, with a much higher growth rate. However, the unconfined mode that was unstable for large  $H$ , while visible as a saddle point, transitions to convective instability, with a negative growth rate. At significant confinement of  $H = 8$ , both the  $S_1$  and  $S_2$  modes are damped as plotted in Fig. 3(d), and are convectively unstable [ $S_1$  is not visible in Fig. 3(d) for this choice of axes].

The corresponding eigenfunctions at the saddle point in the complex plane, representing the streamwise and transverse disturbance function of the  $S_1$  and  $S_2$  modes, are shown in Fig. 4. In Fig. 4(a), at  $H = 30$  the disturbance functions of  $S_1$  appear to be the typical eigenfunctions encountered in unconfined flows, sharply peaking in the shear layer and rapidly decaying on either side. The  $S_2$  mode at  $H = 30$  is qualitatively different; as Healey points out, the admissibility of negative values of  $k$ , due to the presence of the confining wall, implies that slower decay in the transverse ( $y-$ ) direction is possible, and is indeed evident in Fig. 4(b) even for large values of  $H$ . For  $H = 15$ , which is a case with  $S_1$  being convectively unstable and  $S_2$  being the dominant mode, we see that the eigenfunction of  $S_2$  does not appear radically different from the  $S_1$  mode.

Figure 5(a) shows the transition boundary between absolute and convective instability as a result of the emergence of the inviscid  $S_2$  mode (red curve) and subsidence of the  $S_1$  mode (black) as  $H$

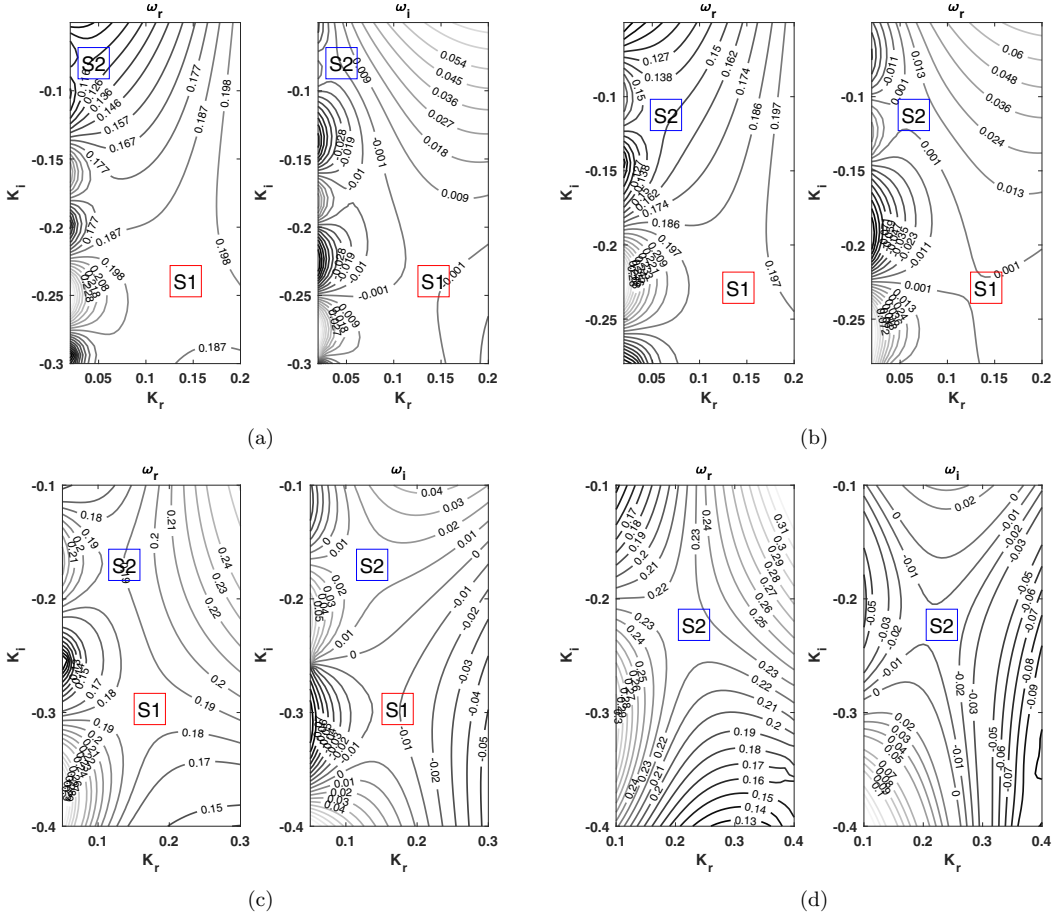


FIG. 3. Emergence and progression of a confined shear layer mode when  $R = 1.315$  as the distance  $H$  of the wall from the shear layer inflection point is reduced on the low-speed side: (a)  $H = 35$ , (b)  $H = 25$ , (c)  $H = 15$ , and (d)  $H = 8$ . Note that the initial instability is due to the free shear layer mode, and the confined mode becomes more unstable as  $H$  is reduced.

is reduced. Points to the left of both curves are convectively unstable. The net effect is to introduce a kink in the stability boundary, at the crossover point between the two modes, with the emergence of the  $S_2$  mode causing shifts in the wavelength of the  $S_1$  mode. Confinement on the low-speed side is destabilizing; decreasing values of counterflowing velocity are required in order to trigger absolute instability for an intermediate range of  $H$ ,  $9.195 < H < 28.127$ . Figure 5(b) shows the wave numbers of the two modes along their A-C transition boundary: it is quite apparent that the  $S_2$  mode is of very long wavelength even when it is technically the more dominant mode, for values of  $H < 28$ , and becomes short ( $k_r > 0.1$ ) only for greater confinement,  $H < 16$ . The implications of the long wavelength of  $S_2$  on the possibility of experimental detection remain unexplored for the moment.

Figures 6 and 7 provide further details on the wavelength and frequency characteristics of the two modes ( $S_1$  and  $S_2$ ), respectively, including behavior away from the A-C transition boundary. It is instructive to consider four regimes, corresponding to large and small  $R$ , and large or small  $H$ . Consider the first case of large values of  $H$ . At large  $H$ , an increase in  $R$  towards large values causes the saddle point location of the  $S_1$  mode to asymptote towards the value for an unbounded

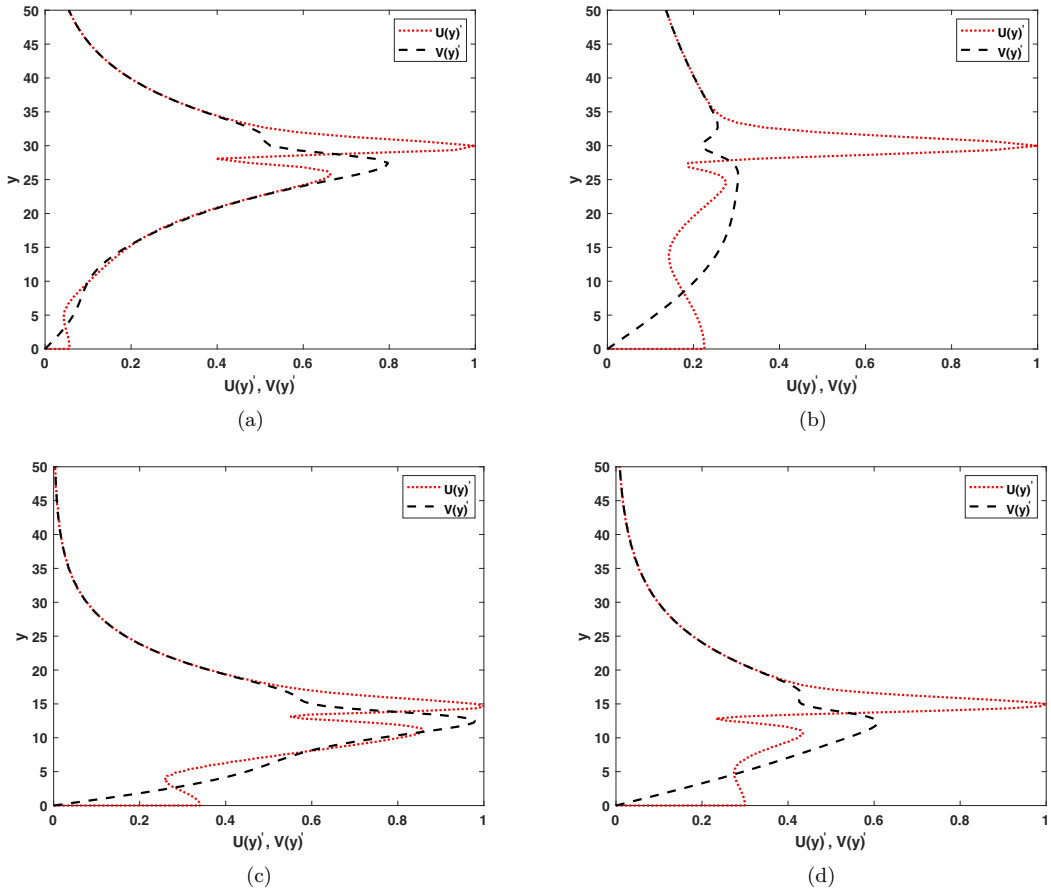


FIG. 4. Eigenfunctions of (a) the free shear layer mode and (b) the confined mode for  $H = 30$ , and (c), (d) for  $H = 15$  when  $R = 1.315$ .

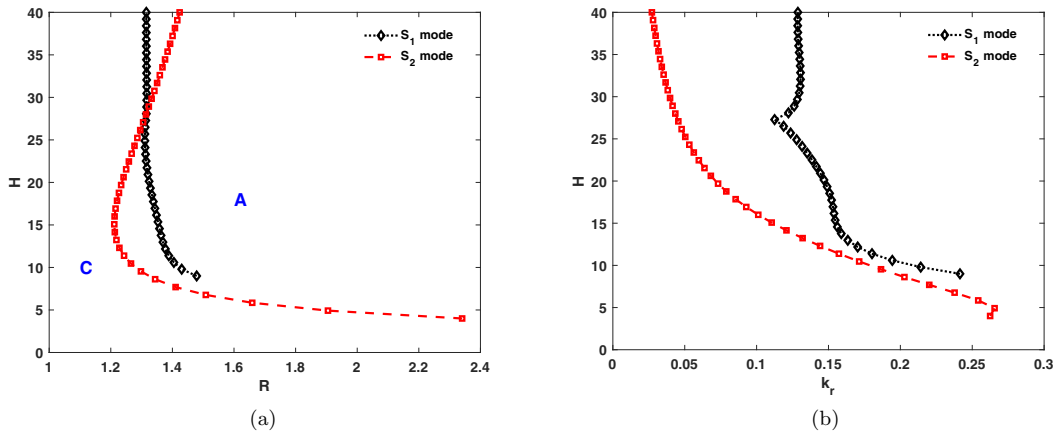


FIG. 5. (a) Absolute-convective transition boundary for the two modes: free shear layer and confined mode, for confinement on the low-speed side. (b) Wave numbers of the two modes along the transition boundary. ( $H$  for the intersection in (a) is 28.12; that for the point in (b) is 27.33.)

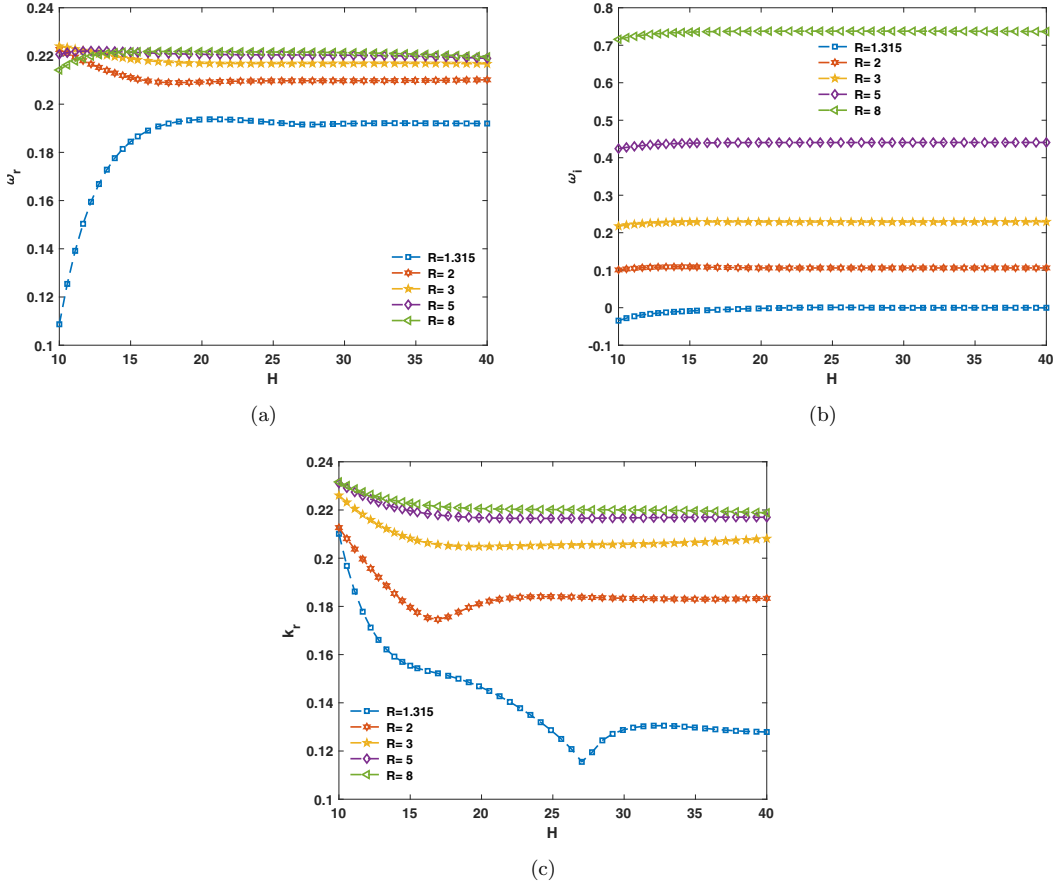


FIG. 6. (a) Frequencies of the saddle point for  $S_1$  modes plotted as a function of the velocity ratio  $R$  and the distance  $H$  of the wall from the shear layer inflection point, (b) temporal amplification rates for saddle point, and (c) wave number of the unstable mode.

shear layer [12],  $k = 0.2225$  and  $\omega = 0.2225$  as expected as shown in Figs. 6(a) and 6(c). Growth rates increase monotonically as  $R$  is increased. For  $R = 1.315$ , the growth rate dips below zero for sufficient confinement but is positive for larger  $R$  as plotted in Fig. 6(b). Turning to the  $S_2$  mode in Fig. 7, a comparison of Figs. 6(c) ( $S_1$  mode) and 7(c) indicates that at large  $H$  and for all values of  $R$ , the wave number of the  $S_1$  mode is larger than 0.1, while the wave number of the  $S_2$  mode is very small, corresponding to long waves. Turning to the case of small  $H$ , the frequency of the  $S_1$  mode for  $R = 1.315$  becomes very low as shown in Fig. 6(a), though the wave number remains not too small, signifying that the phase velocity of the mode is also decreasing towards zero. However, for greater values of  $R$ , the frequency and wave number become relatively insensitive to  $H$ . At the greatest confinement and/or smallest values of  $H$ , the dominant mode is  $S_2$ , with much greater growth rate than  $S_1$ , and it has a relatively short wavelength as plotted in Figs. 6(b) and 7(b).

### B. $R < -1$ : Confinement on the high-speed side

We now turn to velocity profiles with the high-speed stream near the wall ( $R < 0$ ), and explore the effect of confinement. As noted by Healey, confinement on the high-speed side is far more destabilizing than confinement on the low-speed side. This is reflected in the  $A$ - $C$  boundary transition for this configuration, shown in Fig. 8(a). The  $S_2$  mode has an  $A$ - $C$  boundary that is entirely

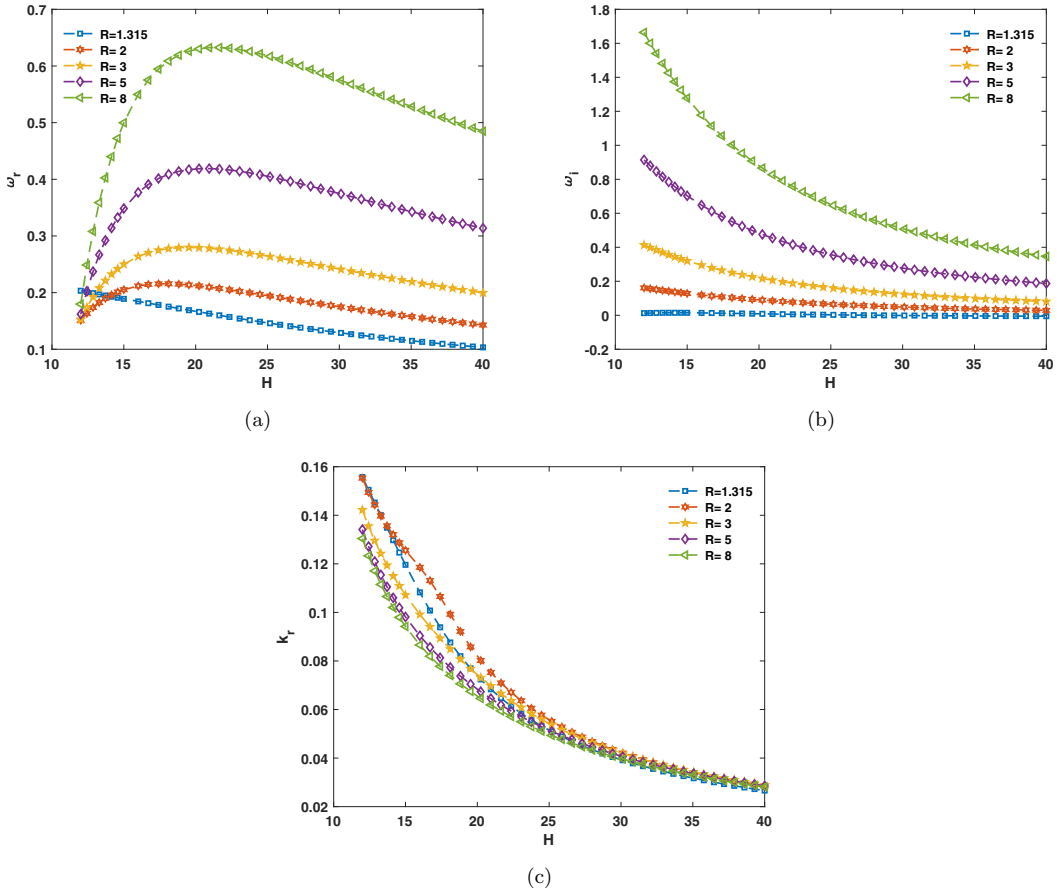


FIG. 7. (a) Frequencies of the saddle point for  $S_2$  modes plotted as a function of the velocity ratio  $R$  and the distance  $H$  of the wall from the shear layer inflection point, (b) temporal amplification rates for saddle point, and (c) wave number of the unstable mode.

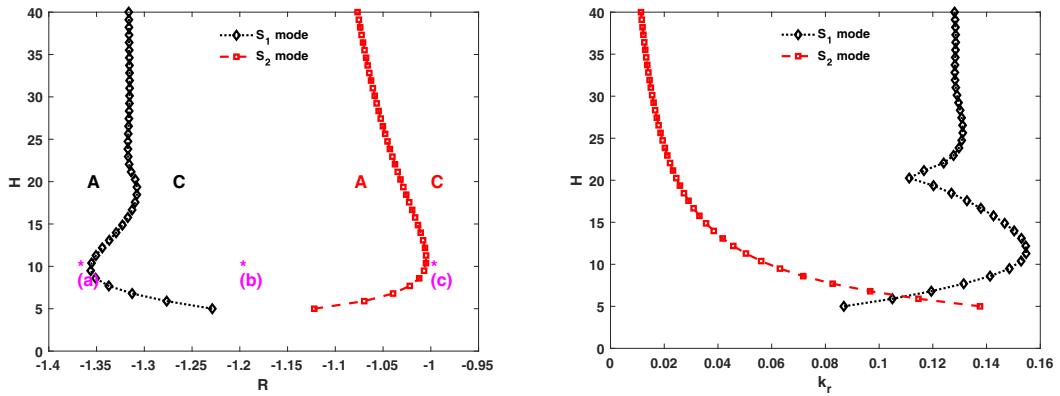


FIG. 8. Left: Absolute-convective transition boundary for the two modes: free shear layer and confined mode, for confinement on the high-speed side. Right: Wave numbers of the two modes along the transition boundary.

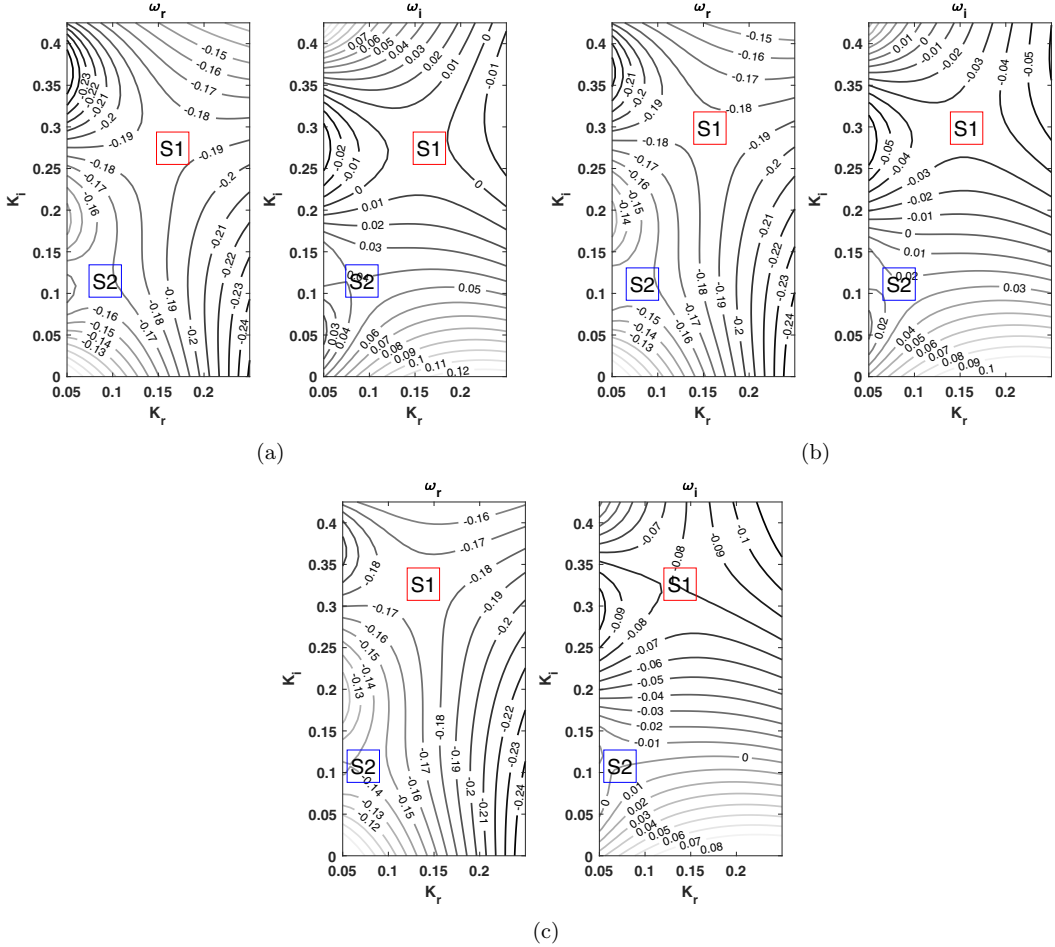


FIG. 9. Emergence and progression of a confined shear layer mode as the distance  $H$  of the wall from the shear layer inflection point is fixed to 10 on the high-speed side: (a)  $R = -1.37$ , (b)  $R = -1.20$ , and (c)  $R = -1.00$ .

to the right of the  $S_1$  mode, indicating that it is always more unstable at all degrees of confinement. The  $S_2$  mode even displays absolute instability at  $R = -0.998$ , i.e., at nearly no counterflow. As was encountered for low-speed confinement, the  $S_2$  mode starts out at long wavelengths in Fig. 8(b) and, as confinement is increased, moves to shorter wavelengths, causing a nonmonotonic behavior of the  $S_1$  mode location in the complex plane. Figure 9 shows the emergence of the  $S_2$  mode in the positive half of the complex wave-number plane as the counterflow parameter  $R$  is varied at a fixed height of  $H = 10$ . The plane is shown for three points in the  $R$ - $H$  parameter space marked (a), (b), and (c) in Fig. 8, corresponding to cases where both modes are absolutely unstable (a), both stable (c), and a case where the  $S_2$  mode is unstable and the  $S_1$  mode is convectively unstable (b). Conversely, if reverse velocities are significantly increased at fixed  $H$  ( $R$  approaching  $-1$ ), the frequency decreases.

Figure 10(a) depicts the real frequency  $\omega_r$  of the saddle point determining the more unstable mode ( $S_2$ ) as a function of  $H$  for various values of  $R$ . Values of  $\omega_r$  are now negative, reflecting the fact that the scaling velocity  $(U_1 + U_2)/2$  is now negative, and the saddle point is now located in the positive  $k_i$  plane. Figures 10(b) and 10(c) show the corresponding growth rate and wave number.

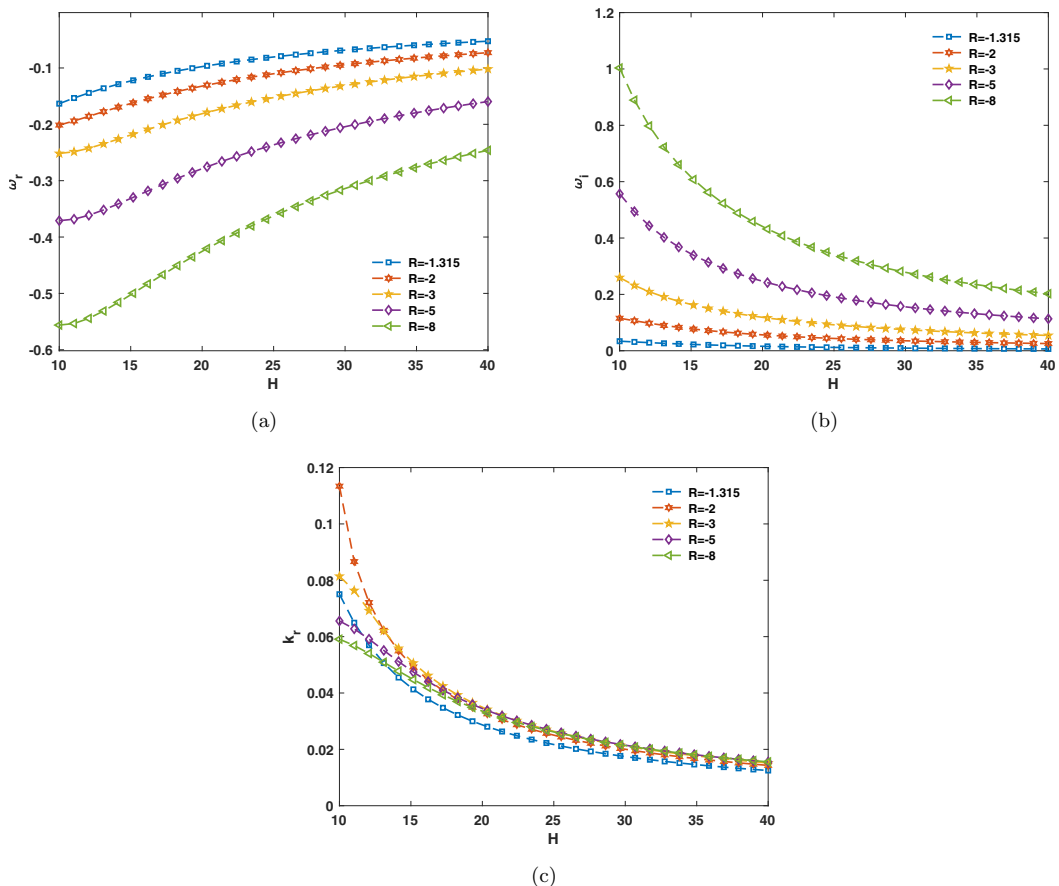


FIG. 10. (a) Frequencies of the saddle point for  $S_2$  modes with varying velocity ratio  $R$  as a function of the distance  $H$  of the wall from the shear layer inflection point with high-speed side confinement, (b) temporal amplification rates for saddle point, and (c) wave number of the unstable mode.

As confinement increases, the unstable frequency increases in magnitude, and the mode goes from a long-wave disturbance to shorter wavelengths [Fig. 10(c)].

In summary, when an inviscid countercurrent shear layer is strongly confined on the low-speed side, the flow is destabilized, with growth rates increasing due to the emergence of a long-wave mode which progressively decreases in wavelength as confinement increases. The effects of confinement on the frequency of the unstable mode are far more significant, with values increasing as counterflow is increased towards  $R = \infty$ . When the counterflow is increased significantly to become the high-speed flow, the confined mode is much stronger, and more unstable at any level of confinement. The frequency decreases as the reverse velocity is increased at fixed confinement.

## V. EFFECT OF WALL BOUNDARY LAYER THICKNESS

The results presented so far were based on an inviscid analysis. We now include the viscous terms in the perturbation equations, with appropriate boundary conditions (see Supplemental Material [23]) and investigate the stability of more realistic velocity profiles. In particular we are interested in the role of the wall boundary layer  $\delta_w$ , in terms of the velocity profile as well as the addition of the no-slip condition. While continuing to use confined shear layer profiles with inflection points located at  $y = H$ , we now assume that the peak reverse velocity  $U_2$  is located at  $y = \delta$ , with  $R$

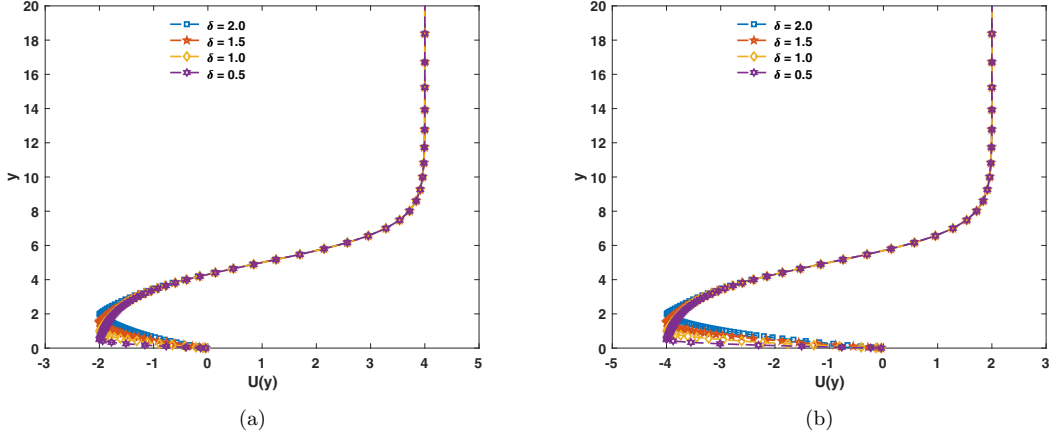


FIG. 11. Velocity profiles considered for evaluating the effects of the wall boundary layer interaction with the countercurrent shear layer for  $H = 5$  and  $\delta = 2, 1.5, 1.0, 0.5$ : (a)  $R = 3$  and (b)  $R = -3$ .

calculated based on this velocity. The velocity profile in the boundary layer is assumed to be a quadratic profile of the form

$$U_{bl} = y(ky - b) \quad (5)$$

with the constraints

$$U_{bl,y=\delta} = 1 + R \tanh\left(\frac{\delta - H}{2}\right) \quad (6)$$

and

$$U'_{bl,y=\delta} = \frac{R}{2} \operatorname{sech}^2\left(\frac{\delta - H}{2}\right), \quad (7)$$

which arise from continuity of the velocity and its derivative at  $y = \delta$ , when matching to the shear layer velocity profiles given by Eq. (2) or Eq. (3). From these, the values of  $k$  and  $b$  are calculated to be

$$k = -\frac{2R \tanh\left(\frac{\delta - H}{2}\right) + \delta R \operatorname{sech}^2\left(\frac{\delta - H}{2}\right) + 2}{2\delta^2} \quad (8)$$

and

$$b = -\frac{4R \tanh\left(\frac{\delta - H}{2}\right) + \delta R \operatorname{sech}^2\left(\frac{\delta - H}{2}\right) + 4}{2\delta}. \quad (9)$$

For values of  $H > 20$ , the wall boundary layer has little interaction with the shear layer except for the largest values of  $\delta$ , and the instability is primarily governed by the free shear layer. As a result, for  $H = 20$  and all values of  $\delta$  considered up to  $\delta = 10$ , there is little effect on the most unstable frequency or growth rate, and the results are not presented. Velocity profiles of Eq. (4) for  $R = \pm 3$  and varying  $\delta$  are shown in Figs. 11(a) and 11(b) for significant confinement,  $H = 5$ . A comparison with the profiles in Fig. 2 suggests that the basic features of the profiles are being captured. The range of measured values of  $\delta_c$  normalized by the momentum thickness lies between 0.7 and 1.6 (Table I), which is slightly extended in the profiles shown in Fig. 11. Further, the measured values

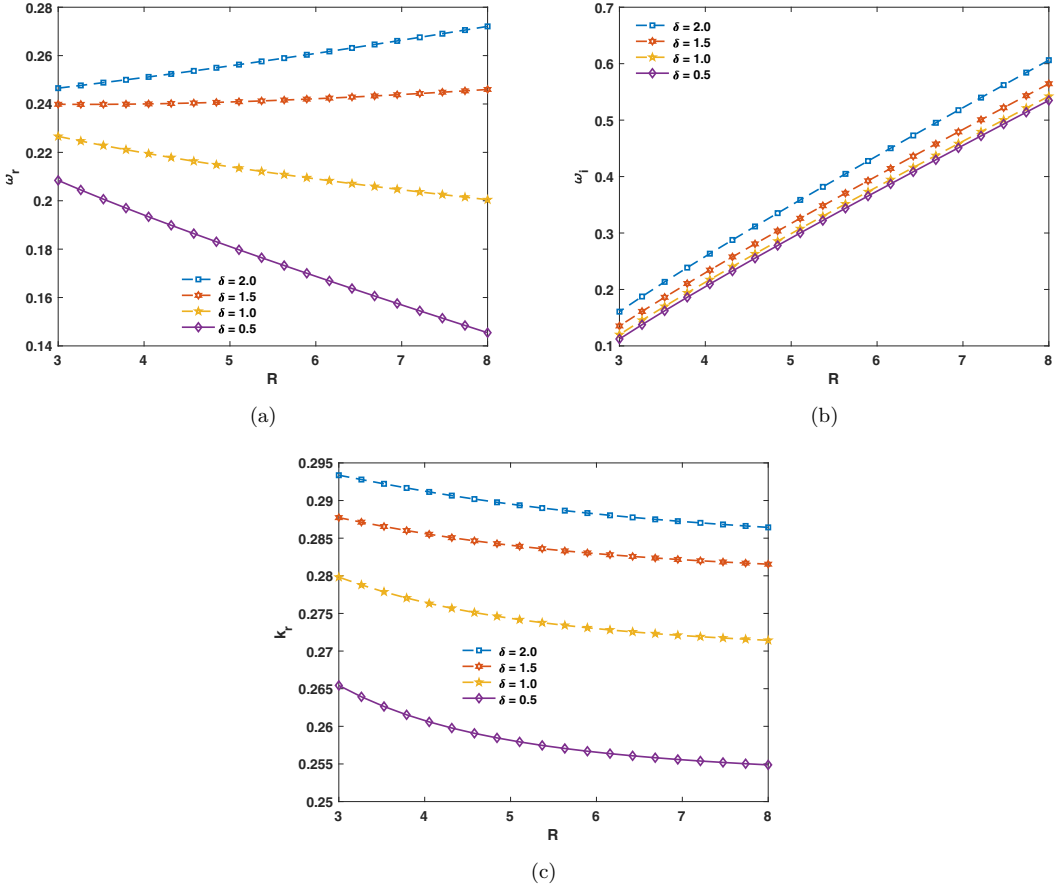


FIG. 12. Response of the dominant mode saddle point to boundary layer development on the wall with  $R > 1$ : (a) unstable frequency, (b) growth rate, and (c) wave number.

of  $\frac{\delta_w}{H}$  lie in a narrow range of  $[0.25, 0.28]$ , which is also covered in these profiles. We, therefore, expect some meaningful translation of the results from these profiles to the measurements.

## Results

Figure 12(c) considers the case of  $R > 1$  and strong confinement ( $H = 5$ ) and shows that the wave number increases very weakly as the boundary layer thickness is increased. There is a weak destabilizing effect on growth rate with increased boundary layer thickness [Fig. 13(b)], likely due to the larger region of velocity gradient and disturbance kinetic energy production. The frequency, on the other hand, shows monotone increasing or decreasing trend with  $R$ , depending on the value of  $\delta$ , likely depending on the location of the critical layer, as altered by the boundary layer profile. Figure 13 shows the saddle point parameters for confinement on the high-speed side. It is interesting to note that the growth rate of the dominant mode is hardly affected by the boundary layer thickness [Fig. 12(b)], attesting to the strength of the inflection-point-driven inviscid instability. The mode frequencies, as for low-speed confinement, may increase or decrease with  $R$ , depending on the value of  $\delta$ . Considering that in an experimental situation, where a value of  $R < -1$  may be attained by a high-speed wall jet, further increases in the wall jet velocity will cause  $R$  to approach  $-1$  from below, while reducing  $\delta$ ; Figs. 13(a) and 13(c) suggest that such an experimental trajectory is likely to lead to a drop in observed frequency and a weakly increased wavelength.

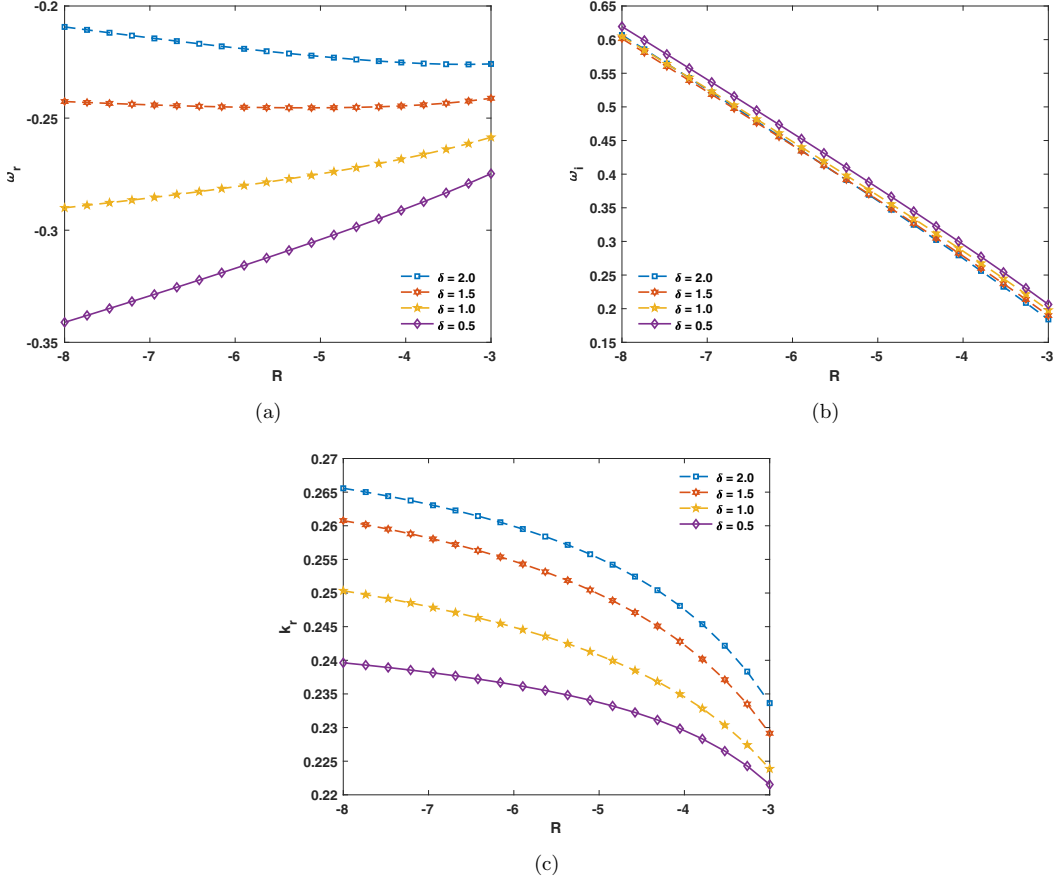


FIG. 13. Response of the unstable mode to boundary layer development on the wall with  $R < -1$ : (a) unstable frequency, (b) growth rate, and (c) wave number.

## VI. COMPARISON WITH EXPERIMENTS

A reexamination of the measured velocity profiles in Fig. 2 clearly shows experimental noise, precluding the profiles from directly being used in stability calculations. Further, the measured velocity profiles do not exactly follow a tanh profile in the shear layer. Attempts to fit the measured velocities as a family of profiles using a combination of tanh and polynomial profiles in different regions (tanh for  $y \geq H$ , polynomials for  $y \leq \delta$  and  $\delta \leq y \leq H$ ) proved unsuccessful. However, it is possible to extract the nondimensional length scales  $\delta$ ,  $H$  corresponding to the dimensional values listed in Table I, normalized by the measured momentum thickness. These are listed in Table II, along with the measured Strouhal number  $f^{\theta}/U$ . A look at Figs. 6 and 7, as well as at Figs. 12 and 13, attests that the values of  $H$  and  $\delta$  listed in Table II are such that neither parameter can be neglected when trying to model the measured velocities with smooth analytical profiles, and need to be represented accurately. Reexamining Table I, we note that normalized values of  $H$  can range from 4 to 14, concurrently with large swings in values of  $R$  from 27.8 to  $-18.8$ , while  $\delta$  stays relatively constant, averaging around 0.27.

We tackle the problem of finding a smooth analytical solution in two parts. Using the values of  $\delta$  calculated from measurements, we can combine the quadratic function of Eq. (4) along with the appropriate base tanh profiles for  $R > 1$  or  $R < -1$ , and would expect to closely approximate

TABLE II. Shear layer and boundary layer parameters evaluated from measured velocity profiles from the experiments of Anderson [22].

Mass flow rate (%)	$R$	$H$	$\delta$	$\frac{f\theta}{U}$	$\frac{\omega_r}{2\pi}$	$k_0$	$\omega_0$
0.090	3.08	5.91	1.72	0.021	0.039	$0.3066 - 0.0914i$	$0.2427 + 0.2500i$
0.14	4.25	4.49	1.32	0.037	0.028	$0.3713 - 0.0064i$	$0.1743 + 0.4631i$
0.18	9.00	3.71	0.94	0.092	0.026	$0.3455 + 0.0919i$	$0.1619 + 1.0100i$
0.23	27.25	3.47	0.89	0.265	0.204	$0.3038 + 0.1109i$	$-1.2829 + 2.7162i$
0.27	-18.85	2.98	0.86	0.099	0.278	$0.2503 + 0.1550i$	$-1.7484 + 1.4438i$
0.32	-8.18	2.70	0.83	0.048	0.161	$0.1910 + 0.1591i$	$-1.0132 + 0.3296i$
0.36	-5.27	2.70	0.83	0.030	0.111	$0.1766 + 0.1579i$	$-0.6971 + 0.1481i$

the experimentally measured profile. However, this turns out not to be the case, with the value of the peak reverse velocity at the  $y$  location,  $y = b/2k$ , not being well approximated. We therefore apply a correction  $\Delta U = 1 - R - Uy = b/2k$  when  $R > 1$  or  $\Delta U = R - 1 - Uy = b/2k$  when  $R < -1$ . In the boundary layer, we now write

$$U(y) = U + \Delta U \exp^{-|y - \frac{b}{2k}|}, \quad (10)$$

which approximates the velocity profiles much better, as shown in Figs. 14(a) and 14(b) for two cases corresponding to injected mass flow rates of 17% and 32%, respectively, which exemplify situations where the near-wall stream has peak velocity magnitudes less than the primary velocity in one instance, and greater in the other instance. Figure 14(c) shows the comparison of the experimentally observed Strouhal numbers with the calculated frequencies of the dominant mode.

While the calculated values qualitatively predict the behavior of the observed frequency, particularly the rise towards the point where  $R$  changes sign, before a decreasing as the mass flow rate increases and  $R$  becomes negative, quantitative agreement is not very good. A variety of arguments may be advanced as to why this might be the case. For example, the experimental frequency spectra are noisy, with a peaked but not too narrow distribution, posing a problem in extracting an unambiguous frequency peak. Further, the choice of streamwise measurement location for use as base profiles is not as obvious for a wall-bounded layer as it may be for, say, the counterflow jet profiles of Strykowski and Niccum [10]. This is because the data in Ref. [22] suggest that the wall jet on the curved surface is not an undisturbed boundary layer. We point out yet another aspect of the velocity profile, namely, that Eq. (9), while approximating the measured velocity profiles well (Fig. 14), does not satisfy the no-slip condition. The reason for this is that the correction used to modify the model profile away from a regular tanh profile towards the experimental profile does not go to zero at the wall, while hewing close to the profile everywhere. Whether this is indeed influential in determining the discrepancy between theory and experiment is arguable; the results for the canonical tanh profile show that a boundary layer thickness of 0.25 does not alter the frequency, and growth rates are sensitive mainly to the counterflow ratio.

We address the question of choice of velocity profile by selecting another set of velocity profiles measured 10 mm downstream of the first location. This is roughly half the wavelength of the unstable mode predicted using the previous set of profiles. A global mode would be expected to establish itself only if velocity profiles do not change drastically over a distance of the order of a wavelength, and therefore we would expect to see similar results as before. The comparisons between the numerical and experimental velocity profiles are shown in Figs. 15(a) and 15(b), while Fig. 15(c) shows the frequency comparison. The comparison actually improves slightly, with the location of the frequency peak being accurately captured as a function of injected mass flow rate, compared to the upstream location.

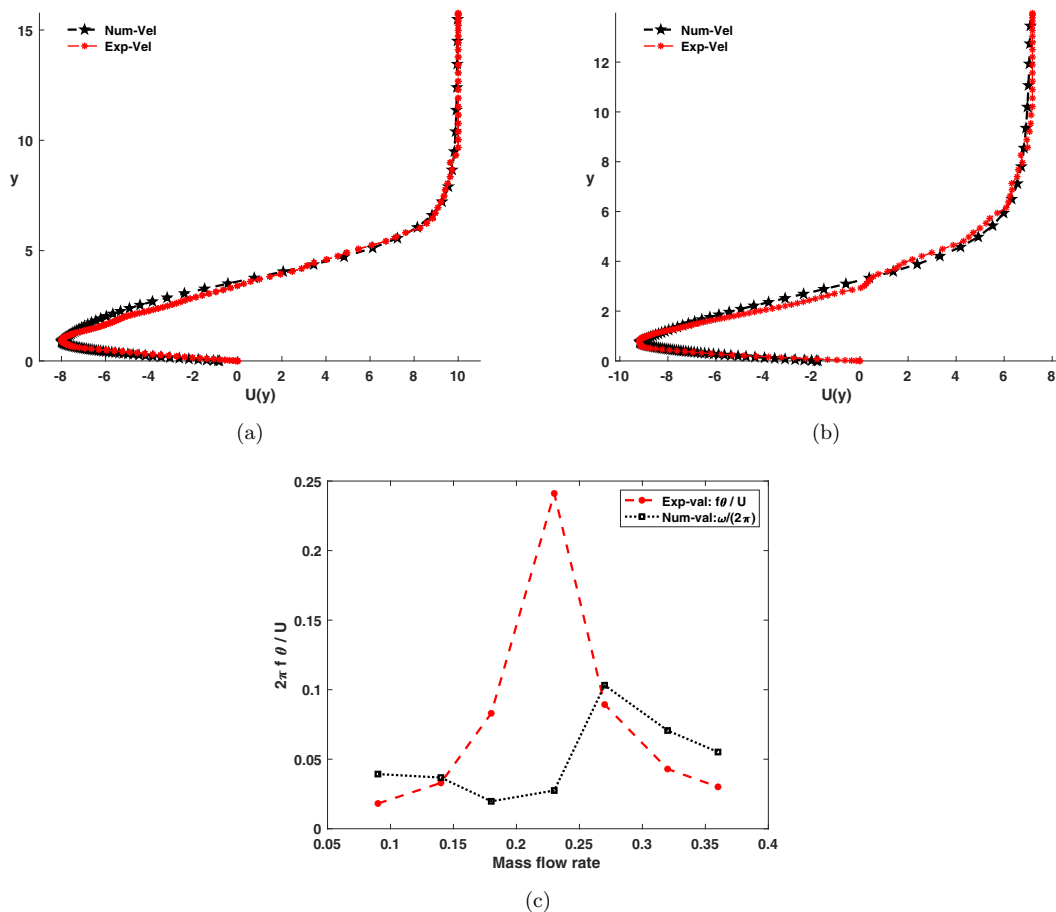


FIG. 14. Measured velocity profiles and corresponding numerical fits for a location immediately downstream of the splitter plate for mass flow rates of (a) 18%, corresponding to low speed confinement, (b) 32%, high speed confinement, and (c) comparison of measured and predicted Strouhal numbers as a function of injected mass flow rate.

Overall, the agreement between the predictions of linear theory for the frequency of absolutely unstable modes and experimentally observed peaks in frequency spectra is very reasonable. Given the reality that the experiments are conducted in a ducted geometry, with attendant streamwise and spanwise pressure gradients, and the injected counterflow jet passes through a region of strong turbulent mixing before it encounters the splitter plate that anchors the primary stream, this agreement is quite significant and points to the strength of linear theory as a robust predictor of the onset and behavior of global modes. The values of the predicted frequency are somewhat sensitive to the choice of velocity profile used, but in such a confined experimental system, it is not clear what the most upstream “wavemaker” profile (to borrow from the terminology of Pier and Huerre [16]) should be. In this study we have insisted on denoting the flow stream with the larger cross section as the primary stream, even when the reverse velocities are larger in some instances. Therefore the most upstream location that may satisfy the conditions for being a wavemaker would be immediately downstream of this stream’s splitter plate, and hence serve as our basis for comparison. However, the higher velocity of the injected flow at downstream locations may cause high shear rates, and correspondingly stronger instabilities. Thus, it is possible that other locations are more appropriate.

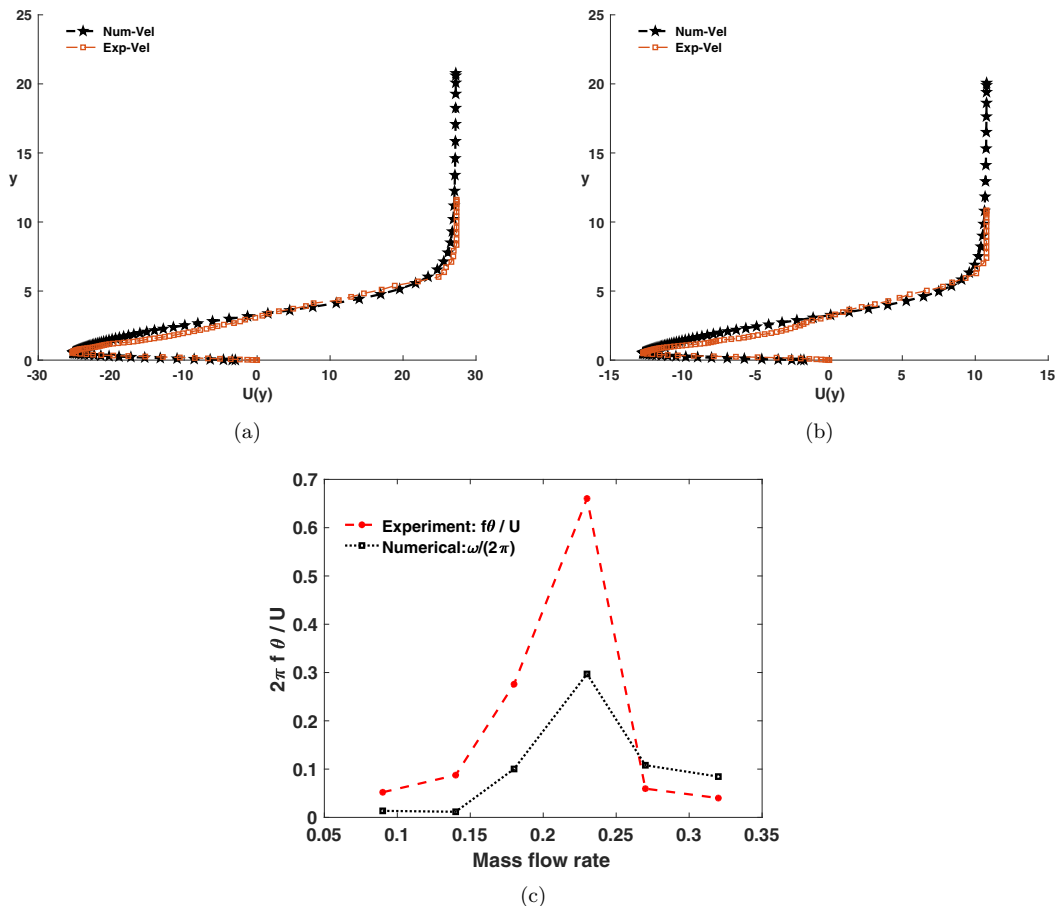


FIG. 15. Measured velocity profiles and corresponding numerical fits for a location  $x = 10$  mm downstream of that used in Fig. 14 for mass flow rates of (a) 23%, corresponding to low speed confinement, (b) 32%, high speed confinement, and (c) comparison of measured and predicted Strouhal numbers as a function of injected mass flow rate.

Nevertheless, a comparison between Figs. 14 and 15 suggests that most locations in this region will yield qualitatively similar results.

## VII. SUMMARY

This study applies spatiotemporal linear stability theory to assess the effects of confinement on a canonical tanh velocity profile. Consistent with previous studies, it is shown that additional long-wavelength modes emerge, that are more unstable than the unconfined modes. Over large regions of the parameter space in  $R$  and  $H$ , these remain long-wavelength modes, even if growth rates are predicted to be greater than the unconfined modes. As confinement is increased, the original unconfined mode transitions to convective instability, and the long-wave modes become the dominant mode, and also become shorter in wavelength. High-speed side confinement is much more destabilizing than confinement on the low-speed side. The insights from the parametric analysis of a tanh profile are used to understand the predictions made using velocity profiles measured in a momentum-driven countercurrent shear layer. The experiments used a wall-bounded secondary stream to create the secondary flow. While the measured velocity profiles deviate from the classical

tanh profile, overall trends in the measured frequency are similar to that of the predicted values of the confined modes. Nondimensionalization of the experimental parameters suggests that confinement effects, while strong, did not change significantly over the experimental parameter space, and that wall boundary layer effects were negligible. As a result, the observed frequencies remain primarily a function of the imposed countercurrent flow.

The results also confirm that momentum-driven flows can be used to create countercurrent shear layers in confined flows, provided that the appropriate conditions are created that prevent the formation of stagnation point flow. For such flows, the observed global mode frequencies are reasonably predicted by linear theory, so long as velocity profiles are used that represent the initial stages of the primary and secondary streams. Additional considerations, such as variable density fields and viscous effects, would need to be considered for application to real situations.

#### ACKNOWLEDGMENTS

We gratefully acknowledge the partial support of the donors to the American Chemical Society-Petroleum Research Fund through Award No. 59791-ND9.

---

- [1] S. A. Ahmed and A. S. Nejad, Velocity measurements in a research combustor part 1: Isothermal swirling flow, *Exp. Therm. Fluid Sci.* **5**, 162 (1992).
- [2] R. W. Pitz and J. W. Daily, Combustion in a turbulent mixing layer formed at a rearward-facing step, *AIAA J.* **21**, 1565 (1983).
- [3] A. A. Behrens and P. J. Strykowski, Controlling volumetric heat release rates in a dump combustor using countercurrent shear, *AIAA J.* **45**, 1317 (2007).
- [4] T. C. Lieuwen and V. Yang, *Combustion Instabilities in Gas Turbine Engines: Operational Experience, Fundamental Mechanisms, and Modeling* (American Institute of Aeronautics and Astronautics, Reston, VA, 2005).
- [5] C. Williamson, Vortex dynamics in the cylinder wake, *Annu. Rev. Fluid Mech.* **28**, 477 (1996).
- [6] D. M. Kyle and K. R. Sreenivasan, The instability and breakdown of a round variable-density jet, *J. Fluid Mech.* **249**, 619 (1993).
- [7] M. D'Oice, J. Martin, N. Rakotomalala, D. Salin, and L. Talon, Convective/absolute instability in miscible core-annular flow. Part 1: Experiments, *J. Fluid Mech.* **618**, 305 (2009).
- [8] T. Loiseleux, J. M. Chomaz, and P. Huerre, The effect of swirl on jets and wakes: Linear instability of the Rankine vortex with axial flow, *Phys. Fluids* **10**, 1120 (1998).
- [9] P. A. Monkewitz, D. W. Bechert, B. Barsikow, and B. Lehmann, Self-excited oscillations and mixing in a heated round jet, *J. Fluid Mech.* **213**, 611 (1990).
- [10] P. J. Strykowski and D. L. Niccum, The stability of countercurrent mixing layers in circular jets, *J. Fluid Mech.* **227**, 309 (1991).
- [11] M. Provansal, C. Mathis, and L. Boyer, Bénard-von Kármán instability: Transient and forced regimes, *J. Fluid Mech.* **182**, 1 (1987).
- [12] P. Huerre and P. A. Monkewitz, Absolute and convective instabilities in free shear layers, *J. Fluid Mech.* **159**, 151 (1985).
- [13] P. Huerre and P. A. Monkewitz, Local and global instabilities in spatially developing flows, *Annu. Rev. Fluid Mech.* **22**, 473 (1990).
- [14] J.-M. Chomaz, Global instabilities in spatially developing flows: Non-normality and nonlinearity, *Annu. Rev. Fluid Mech.* **37**, 357 (2005).
- [15] J.-M. Chomaz, P. Huerre, and L. G. Redekopp, A frequency selection criterion in spatially developing flows, *Stud. Appl. Math.* **84**, 119 (1991).
- [16] B. Pier and P. Huerre, Nonlinear self-sustained structures and fronts in spatially developing wake flows, *J. Fluid Mech.* **435**, 145 (2001).

- [17] A. Bers, Space-time evolution of plasma instabilities-absolute and convective, in *Basic Plasma Physics: Selected Chapters, Handbook of Plasma Physics, Volume 1* (North-Holland, Netherlands, 1983), p. 451.
- [18] R. J. Briggs, *Electron-Stream Interaction with Plasmas* (MIT Press, Cambridge, MA, 1964).
- [19] J. A. C. Humphrey and S. Li, Tilting, stretching, pairing and collapse of vortex structures in confined counter-current flow, *J. Fluids Eng.* **103**, 466 (1981).
- [20] D. J. Forliti and P. J. Strykowski, Controlling turbulence in a rearward-facing step combustor using countercurrent shear, *J. Fluids Eng.* **127**, 438 (2005).
- [21] D. J. Forliti, B. A. Tang, and P. J. Strykowski, An experimental investigation of planar countercurrent turbulent shear layers, *J. Fluid Mech.* **530**, 241 (2005).
- [22] M. J. Anderson, Global dynamics of a dump combustor using momentum-driven countercurrent shear control, Ph.D. thesis, University of Minnesota, 2011.
- [23] M. P. Juniper, The effect of confinement on the stability of two-dimensional shear flows, *J. Fluid Mech.* **565**, 171 (2006).
- [24] P. W. Bearman and M. M. Zdravkovich, Flow around a circular cylinder near a plane boundary, *J. Fluid Mech.* **89**, 33 (1978).
- [25] J. J. Healey, Destabilizing effects of confinement on homogeneous mixing layers, *J. Fluid Mech.* **623**, 241 (2009).
- [26] M. P. Juniper and S. M. Candel, The stability of ducted compound flows and consequences for the geometry of coaxial injectors, *J. Fluid Mech.* **482**, 257 (2003).
- [27] W. Koch, Local instability characteristics and frequency determination of self-excited wake flows, *J. Sound Vib.* **99**, 53 (1985).
- [28] M. P. Juniper, The full impulse response of two-dimensional jet/wake flows and implications for confinement, *J. Fluid Mech.* **590**, 163 (2007).
- [29] C. Arratia, S. Mowlavi, and F. Gallaire, Absolute/convective secondary instabilities and the role of confinement in free shear layers, *Phys. Rev. Fluids* **3**, 053901 (2018).
- [30] C. D. Winant and F. K. Browand, Vortex pairing: The mechanism of turbulent mixing-layer growth at moderate Reynolds number, *J. Fluid Mech.* **63**, 237 (1974).
- [31] P. Brancher and J.-M. Chomaz, Absolute and Convective Secondary Instabilities in Spatially Periodic Shear Flows, *Phys. Rev. Lett.* **78**, 658 (1997).
- [32] K. Manoharan and S. Hemchandra, Absolute/convective instability transition in a backward facing step combustor: Fundamental mechanism and influence of density gradient, *J. Eng. Gas Turbines Power* **137**, 1 (2015).
- [33] See Supplemental Material at <http://link.aps.org/supplemental/10.1103/PhysRevFluids.6.073901> for description of governing equations used, the formulation of the eigenvalue problem, the Chebyshev collocation solution procedure, and numerical tools used.